Achieving ultra-high bearing strength of tungsten nanoribbons in a transforming metal matrix

Fangmin Guo[a], Shijie Hao[*,a], Xiaohua Jiang[a,b], Daqiang Jiang[a], Lishan Cui[*,a,b], Yang Ren[c]

[a] State Key Laboratory of Heavy Oil Processing, China University of Petroleum, Beijing 102249, China

[b]Beijing Key Laboratory of Failure, Corrosion, and Protection of Oil/Gas Facilities, China University of Petroleum Beijing, Beijing, 102249, China

[c]X-ray Science Division, Argonne National Laboratory, Argonne, Illinois 60439, USA

ABSTRACT:

Nanowires (or nanoribbons) were identified as the most potential structural reinforcements for composites due to their ultrahigh strength, but it is difficult to transcribe their ultrahigh strength into composite. Here, an *in-situ* W nanoribbbons-NiTi matrix composite was fabricated by mechanical reduction of a W-NiTi ingot, and the micromechenical deformation behavior was studied by *in-situ* high energy X-ray diffraction during tensile loading-unloading. It is revealed that the large elastic deformation of the W nanoribbons in a NiTi matrix is dictated by and synchronized with the martensitic transformation of the matrix. The bearing strength of the W nanoribbons, up to 11.6 GPa, was achieved in this composite. A significant load transfer took place from the matrix to the nanoribbons, exhibiting the characters of locality and rapidity. The stress fraction carried by the W nanoribbons with the volume fraction of 3% is up to 45% for the strength of the composite.

KEYWORDS：Tungsten Nanoribbons, Shape Memory Alloy, High Energy X-ray Diffraction, Martensitic Transformation, Bearing Strength

1. Introduction

The mechanical performance of the composites reinforced with one-dimensional (1-D) structural reinforcements strongly depends on the bearing strength of reinforcements [1,2]. It is regarded that the bearing strength mainly depends on the intrinsic load carrying capacity of reinforcements and the load transfer capacity from matrix to reinforcements [3,4]. Nanowires (or nanoribbons) were identified as one of the most potential 1-D structural reinforcements, since their ultrahigh strength [5–8] can render ultrahigh load carrying capacity, and the large long-diameter ratio and the high specific surface area can efficiently contribute to high load-transfer efficiency [9,10]. Many researches have been performed to exploit the high bearing strength of nanowires embedded in bulk composites, aiming to achieve exceptional mechanical properties of the composites [11–13]. However, most of the results obtained are far away from expectation [14,15]. The reasons are usually attributed to the inadequate dispersion, imperfect alignment of the nanowires [16] and the poor interface bonding [17,18], significantly hindering the load transfer from matrix to nanowires [19].

It is reported that for an *in-situ* Cu-Nb nanocomposite wire [20], where the Nb nanowires are well dispersed and aligned in Cu matrix with well-bonded interfaces, the maximum elastic strain of Nb nanowires achieved is just 1.5%. It is calculated that the bearing strength of Nb nanowires is 1.4 GPa ($\sigma_{max}\approx1.5\%\times93$ GPa), far below what may be expected of the freestanding nanowires [6]. This result implies that in addition to the above-mentioned reasons, there should be other critical reasons for the deficiency of the ultrahigh bearing strength of nanowires in this type of composite where the metal matrix plastically deforms by dislocation slip. For this, we considered that the highly localized lattice distortion induced by the dislocations in conventional metal matrix easily triggers large strain mismatch at the nanowire-matrix interfaces, in turn

resulting in the high local stress concentration and causing premature local plastic deformation of the nanowires [21,22]. Consequently, the ultrahigh bearing strength of the nanowires cannot be achieved in the conventional composite design strategy. This drawback hinders the further improvement of mechanical properties of the nanowires reinforced metal matrix composites.

We recently proposed a new concept of "lattice strain matching" at atomic scale between the stress-induced martensitic transformation (SIMT) distortion (~8%) of metal matrix [23] and the elastic strain of nanowires (4-7%) [6,7]. Instead of deforming by dislocation slip, SIMT deformed via lattice shearing of the transforming metal matrix, which can uniformly distribute stress on the nanowires and expel stress concentration at the nanowire-matrix interfaces, thus favoring to exploit the ultrahigh bearing strength of the embedded nanowires [24]. Based on this concept, the ultra-large elastic strains (4.2~6.5%) of Nb nanowires were achieved in NiTi matrix which deformed by the SIMT, rendering the composites with extraordinary mechanical properties [22]. It is known that the bearing strength of nanowires depends on the product of the elastic strain limit and the Young's modulus. Unfortunately, Nb nanowires in the transforming metal matrix can exhibit the ultra-large elastic strain of 6.5%, but their bearing strength is still relatively low due to their low Young's modulus (87 GPa [25]), which is about 5.65 GPa (6.5%×87 GPa). To our knowledge, W has the highest Young's modulus in all reported metals, up to 400 GPa [26], over four times as high as that of Nb. It is envisioned that the W nanowires in the transforming metal matrix might also display an ultra-large elastic strain in the transforming metal matrix and possess the gigantic bearing strength.

In this study, we designed and fabricated an *in-situ* W-nanoribbons/NiTi-matrix composite. It is revealed that the ultrahigh bearing strength of the W nanoribbons, up to 11.6 GPa, was

achieved in this composite. It is found that the stress fraction carried by the W nanoribbons with the volume fraction of 3% is up to 45% for the strength of the composite.

2. Materials and methods

2.1 Material

An ingot of 7 kg with a composition of $Ni_{48.5}Ti_{48.5}W_3$ (at. %) was prepared by means of vacuum induction melting. Since W has an ultrahigh melting point of ~3400℃ and cannot be directly melted with NiTi, the commercial Ni-20 at.%W alloy was selected to provide the W component instead of pure W due to its lower melting point (~1600℃). The raw materials used here were of commercial purity Ni (99.96 wt.%), Ti (99.90 wt.%) and Ni_4W (99.90 wt.%), supplied by Beijing Purui Advanced Material Technology Co. Ltd. and Beijing Tian-Long Tungsten & Molybdenum Co. Ltd. The ingot was hot forged at 850 °C into a bar of 8 mm in diameter and then hot-drawn into a thick wire of 1.4 mm. Finally, the hot-drawn wire was cold-drown into a thin wire of 0.25 mm in diameter with intermediate annealing at 700℃. The test samples were cut from this thin wire and subsequently annealed at 450℃ for 20 min followed by air cooling.

2.2 Methods

High-energy X-ray diffraction (HE-XRD) was carried out at the 11-ID-C beamline of the Advanced Photon Source (Argonne National Laboratory, IL). In-situ uniaxial tensile testing was performed by a screw-driven loading system operated in displacement control. The sample macroscopic stress was recorded by an Omega load cell. The general experimental setup is shown in Fig. 1. The wire specimen was irradiated by a parallel beam of 105.698 KeV photons (corresponding to a wavelength of λ, 0.1173 Å), with approximate dimensions 0.5 × 0.5 mm^2.

Complete Debye rings from the SMA matrix and the W nanowires were recorded using a 2D Perkin-Elmer amorphous silicon detector at a distance of 1700 mm behind the sample, operating in full mode and providing a pixel size of 200×200 μm^2 with 16 bit dynamic range. Otherwise, Pure CeO2 powder (NIST Standard Reference Material SRM-674a), positioned the same place as the sample wire, was used to calibrate the sample-detector distance and other relevant parameters, such as the accurate beam center and detector tilt.

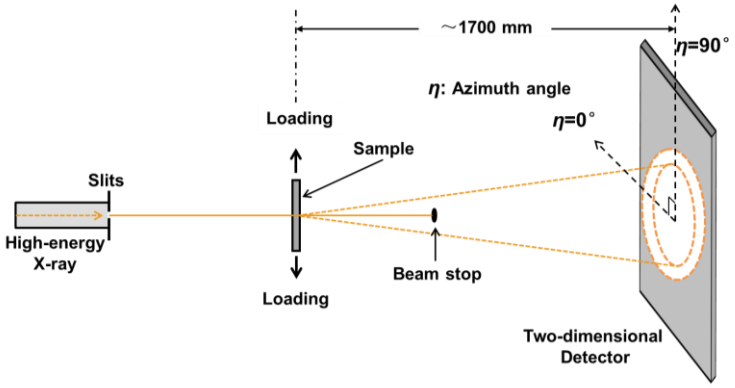

Figure 1 Schematic of experimental *in-situ* tensile setup at 11-ID-C, APS, ANL

The methodology used here to calculate strains and stresses from the Debye ring patterns is similar to those from Refs [27,28]. Each diffraction spot or ring corresponds to the specific crystallographic direction while the azimuthal angle (η) depends on the orientation of the set of planes relative to the sample wire. Such as, 1D diffraction patterns of the sample perpendicular to the stretching direction can be obtained at the angle of 90°, and transverse direction at 0°. For selected crystallographic reflection, the Bragg peaks were fitted using a Gaussian function to find the peak positions which are corresponding to the interplanar spacing (d_η) of different crystallographic directions. Then if applied macro-strains were present, the relationship between the lattice strain of the diffracting crystallites in a specific azimuthal direction and the shift of the

peak positions can be described by: $\varepsilon^{hkl}=(d^{hkl}-d_0^{hkl})/d_0^{hkl}$, where d_0^{hkl} is the interplanar spacing when the sample is under strain-free condition.

3. Results and discussion

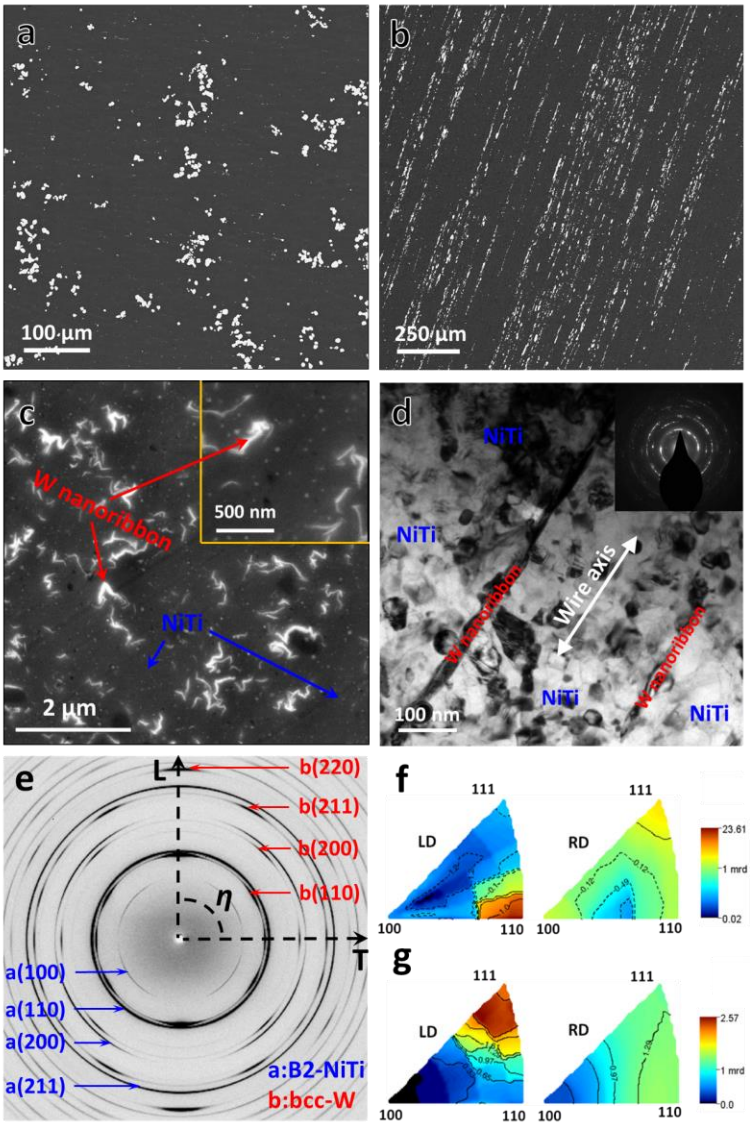

Figure 2. Microstructure of the W-nanoribbons/NiTi-matrix composite. (a) Backscattered electron microscopy (BSEM) image of the NiTi-W ingot (bright regions, W; dark regions, NiTi). (b) BSEM image of the longitudinal section of the forged NiTi-W alloy bar; (c) BSEM observation of the cross section (Inset: higher-magnification view). (d) TEM observation of a longitudinal section (Inset: the corresponding selected area electron diffraction

(SAED)). (e) 2-D HE-XRD spectra. (f-g) Inverse pole figures of W nanoribbons and NiTi matrix (LD is the longitudinal direction and RD is the radial direction).

Fig. 2a shows the SEM image of the NiTi-W ingot, consisting of W micro-particles dispersed into the NiTi matrix. Then W micro-particles were stretched into slender shape by forging, shown in Fig. 2b. Finally, the W micro-strips were dawned into nanoribbons, which have twist cross-sections with 30-60 nm in thickness and 100-1000 nm in width, and a mean aspect ratio exceeding 50, as shown in Fig. 2c. The volume fraction of W nanoribbons is ~3%, estimated from BSEM observations. The W nanoribbons are well dispersed and aligned along wire axial direction in the NiTi matrix, shown in Fig. 2d. Transmission electron microscopy (TEM) image indicates that the grain sizes of NiTi matrix are ranging from 40 nm to 80 nm. HE-XRD pattern of the composite without applied stress, shown in Fig. 2e, can be fully indexed to a body-centered cubic (bcc) W and a B2 austenitic phase NiTi. The uneven distribution of diffraction intensity along the Debye-Scherrer rings in the pattern indicates that both the W nanoribbons and NiTi matrix have the crystal textures. Inverse pole figures in Fig. 2f-g show that the W nanoribbons have a strong <110> fiber texture while the B2-NiTi matrix has a week <111> texture along wire longitudinal direction. Hence, the elastic strain of the W nanoribbons along loading direction can be indicated by the lattice strain of the W (110) perpendicular to the wire axial direction.

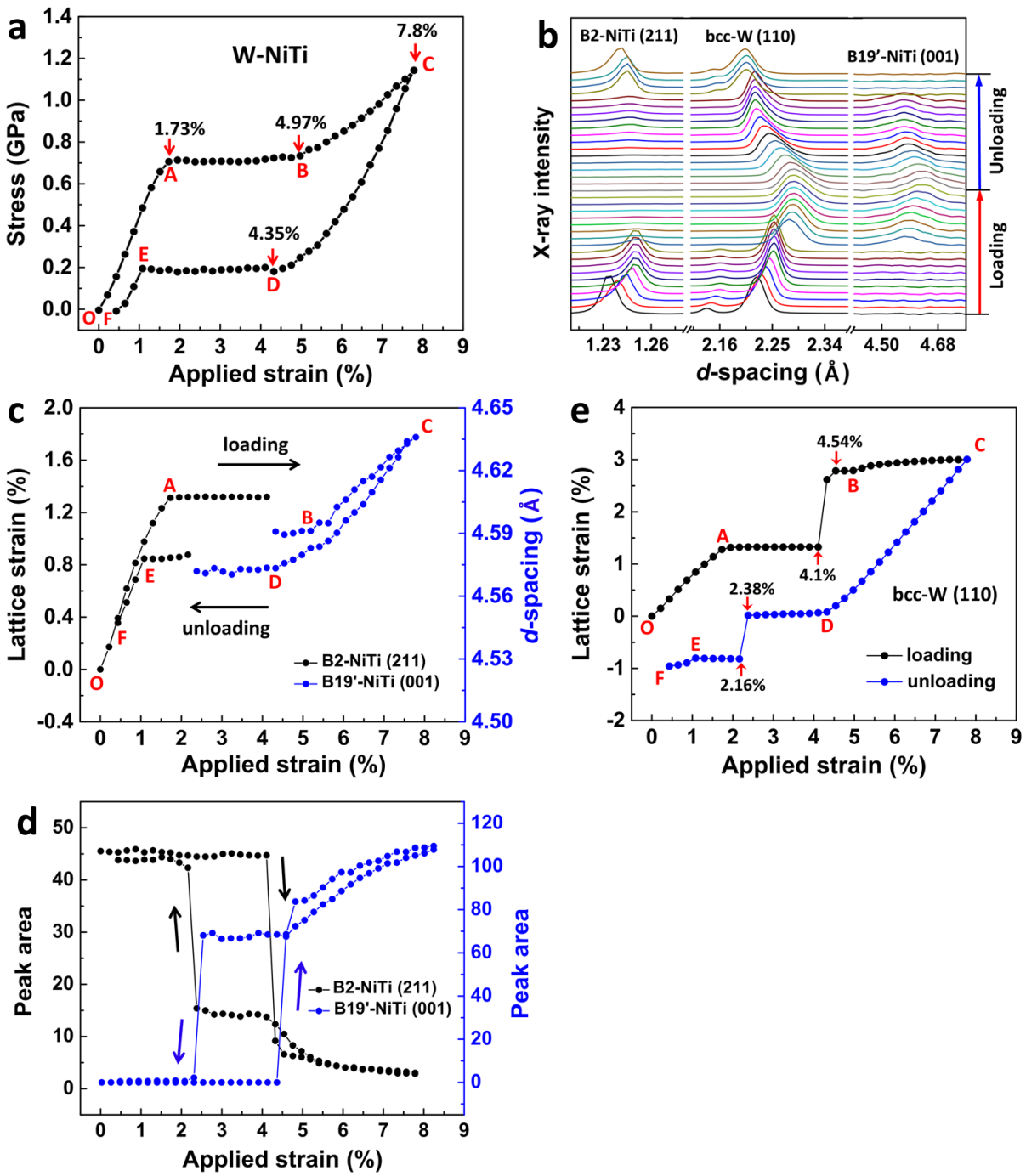

Figure 3. *In-situ* HE-XRD results of the composite during tensile loading-unloading. (a) The macroscopic stress-strain curve of the composite. (b) Evolution of the diffraction peaks of W (110), B2-NiTi (211) and B19'-NiTi (001) perpendicular to the loading direction. (c) Evolution of B2-NiTi (211) lattice strain and B19'-NiTi (001) *d*-spacing

perpendicular to the loading direction. (d) Evolution of the diffraction peak area of NiTi-B2 (211) and NiTi-B19'(001) peaks. (e) Evolution of the lattice strain of W (110) perpendicular to the loading direction.

Fig. 3a presents the stress-strain curve of the composite with applied strain of 7.8%. According to the curve shape, the loading curve may be divided into three stages (O-A, A-B and B-C) and the unloading curve may also be divided into three stages (C-D, D-E and E-F). It is evident that the composite exhibits a typical pseudo-elastic deformation with upper and lower stress plateaus, similar to that of pseudoelastic binary NiTi alloy. The stress of the upper plateau is of 700 MPa and the stress of the lower plateau is of 200 MPa, thus consequent on a large stress hysteresis of 500 MPa. It is noted that both of the lengths of the upper (A-B) and lower (D-E) stress plateaus of the composite are ~3.3%, much shorter than those of conventional NiTi (6-8%). Fig. 3b shows the *in-situ* 1D diffraction spectrums recorded in the longitudinal direction of the composite during the tensile loading and unloading. Fig. 3c shows the evolutions of B2-NiTi (211) lattice strain and B19'-NiTi (001) *d*-spacing along the loading direction with respect to the applied strain. Since the B19'-NiTi phase formed originally during tensile loading was subjected to a tensile stress, the *d*-spacing value of the original B19'-NiTi phase cannot be served as the reference value (d^0) [29]. The B19'-NiTi (001) *d*-spacing instead of lattice strain was used in this study. Fig. 3d shows the diffraction peak areas of B2-NiTi (211) and B19'-NiTi (001) versus the applied strain.

During the initial loading stage (O-A), the lattice strain of B2-NiTi (211) linearly increased by 1.31% with increasing applied strain, reflecting the tensile elastic deformation of the NiTi matrix. With increasing applied strain from point A to 4.1% in stage A-B, both the lattice strain and diffraction peak area of B2-NiTi (211) remained almost constant. With continuous loading from 4.1% to 4.54%, the B2-NiTi (211) diffraction peak abruptly disappeared and the B19'-NiTi

(001) diffraction peak appeared. After that, the B19'-NiTi (001) diffraction peak remained constant. These observations indicate that the NiTi matrix underwent the stress-induced martensitic transformation (B2→B19') in the Lüders-like manner in the upper stress plateau (stage A-B) [30], where the martensitic transformation in the matrix did not occur at the X-ray observation point until the deformation from 4.1% to 4.54%. When the applied strain increased to the end of the upper stress plateau (Point B), it is seen that the B2-NiTi (211) diffraction peak did not completely disappear, as shown in Fig. 3b. It indicates that a portion of B2-NiTi phase in the matrix was retained, which should be the feasible reason for the shorter length of the upper stress plateau (stage A-B in Fig 3a). In stage B-C, the *d*-spacing of B19'-NiTi (001) gradually increased with increasing the applied strain (Fig. 3c), indicating the elastic lattice elongation of B19'-NiTi phase. At the same time, the area of B2-NiTi (211) peak decreased continually by ~20%, conversely the area of B19'-NiTi (001) peak further increased by the same mass (Fig. 3d). These indicate that the retained B2-NiTi phase gradually transformed into B19'-NiTi phase with increasing the applied strain in the stage B-C.

During the unloading stage C-D, both the *d*-spacing and peak area of B19'-NiTi (001) gradually decreased with decreasing the applied strain, while the peak area of B2-NiTi (211) gradually increased (Fig. 3c-d). These suggest that the NiTi matrix underwent simultaneously the tensile elastic recovery and the reverses martensitic transformation to some extent in the initial unloading stage. These observations are different from those of the reported binary NiTi that usually only underwent the tensile elastic recovery in this stage [30]. When unloading to the beginning of the lower stress plateau (point D), a portion (~30 vol.%) of B19'-NiTi matrix had undergone the reverse martensitic transformation (B19'→B2), which leads to the shorter length of the lower stress plateau. During unloading from 4.35% (Point D) to 2.38%, the *d*-spacing and

peak area of B19'-NiTi (001), and the peak area of B2-NiTi (211) almost remained constant. With continuous unloading from 2.38% to 2.16%, the B19'-NiTi (001) peak abruptly disappeared and the peak area of B2-NiTi (211) rapidly increased, as shown in Fig. 3d. After that, both the lattice strain and peak area of B2-NiTi (211) remained constant. These results indicate that the NiTi matrix underwent the reverse martensitic transformation in the Lüders-like manner in the lower stress plateau (stage D-E), where the reverse transformation in the matrix did not occur at the X-ray observation point until the unloading from 2.38% to 2.16%. In the final unloading stage E-F, the B2-NiTi (211) lattice strain decreases linearly with decreasing applied strain, reflecting the tensile elastic recovery of the matrix. At the end of unloading (Point F), the tensile elastic strain of 0.35% was retained in the matrix along the loading direction, indicating that the matrix was subjected to the internal tensile stress from the nanoribbons after the unloading.

Fig. 3e shows the evolution of W (110) lattice strain along the loading direction with respect to the applied strain. During the initial loading stage (O-A), the lattice strain of W (110) linearly increased by 1.32% with increasing applied strain, reflecting the tensile elastic deformation of the W nanoribbons. With increasing applied strain from 1.73% to 4.1% in stage A-B, the tensile lattice strain remained almost constant. With continuously increasing applied strain from 4.1% to 4.54%, the tensile lattice strain of the W nanoribbons showed a sudden increase from 1.32% to 2.78%. The increment is up to $\Delta\varepsilon_{LS}^{\uparrow}$ =1.46%, which is more than 3 times larger than that of the applied strain (4.54%-4.1%=0.44%) over the same period. It is evident that the sudden increase of the lattice strain of the W nanoribbons coincided with the decrease of B2-NiTi (211) diffraction peak and the appearance of B19'-NiTi (001) diffraction peak, as shown in Fig. 3c. These results explicitly demonstrate that the occurrence of the large lattice strain of the W

nanoribbons was dictated by the stress-induced martensitic transformation of the NiTi matrix. Because the martensitic transformation of the NiTi matrix has locality and rapidity, the large elastic deformation of W nanoribbons in the matrix also exhibits these two characteristics, which is quite different from the elastic deformation behavior of freestanding nanowires. With increasing applied strain from B to C, the lattice strain of the W nanoribbons increased by 0.22%, much smaller than the applied strain (7.8%-4.97%=2.83%), indicating that the W nanoribbons underwent a proportion of tensile plastic deformation in this deformation stage.

During the unloading stage C-D, the W nanoribbons performed a tensile elastic recovery. After that, with unloading from 4.35% to 2.38% in stage D-E, the W (110) lattice strain remained almost constant. With decreasing applied strain from 2.38% to 2.16%, the W nanoribbons suddenly suffered a compressive strain of $\Delta\varepsilon_{LS}^{\downarrow}$ = -0.83%, near 4 times larger than the change of the applied strain (2.38%-2.16%=0.0.22%). It is seen that the decrease of the lattice strain of the W nanoribbons firmly accompanied with the reverse martensitic transformation of the NiTi matrix, as shown in Fig. 2d-e, demonstrating that the decrease in the lattice strain of the W nanoribbons is dictated by the reverse martensitic transformation of the NiTi matrix. During unloading from 2.16% to 1%, the W (110) lattice strain remained almost constant. At the end of the unloading (point F), it is apparent that the W nanoribbons sustained a compressive lattice strain of -0.95%. This result can be understood that the plastically extended W nanoribbons hindered the recovery of the NiTi matrix because of the reverses martensitic transformation during the unloading, which caused the large residual compressive elastic strains in the nanoribbons and the residual tensile elastic strains in the matrix.

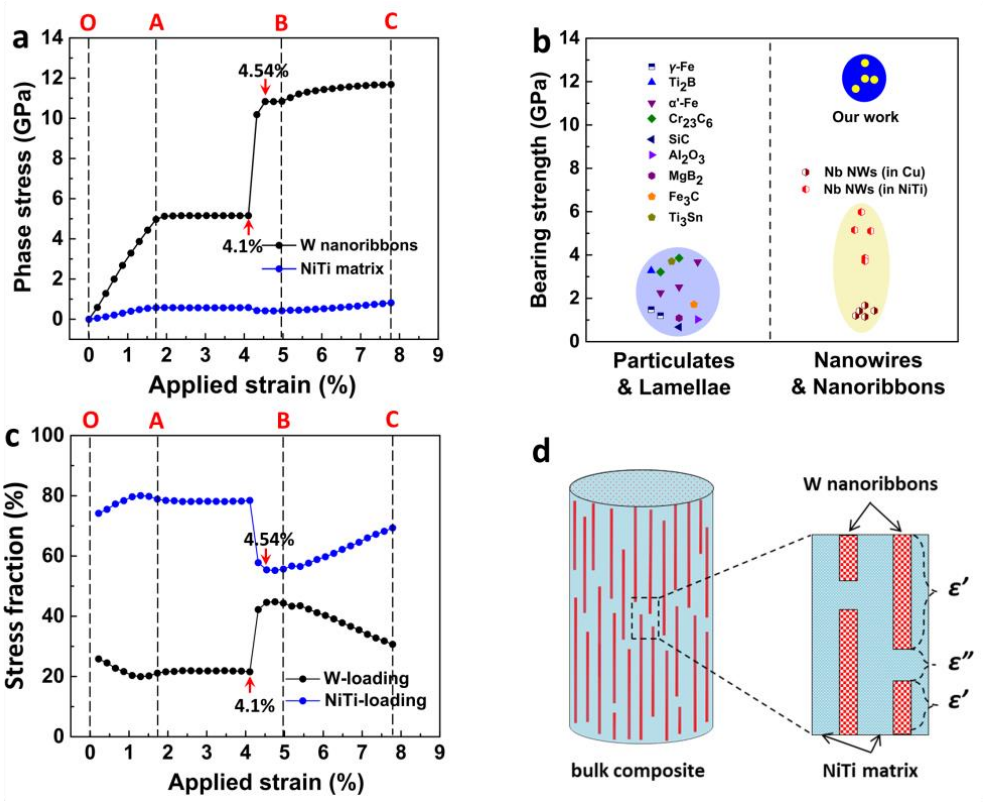

Figure 4. (a) Evolution of the phase bearing stress of the W nanoribbons and the NiTi matrix upon the tensile loading; (b) Comparison of the phase bearing strength of the W nanowires achieved in this composite with those of other hard inclusions (including particulates [31,32], lamellae [24,33–36], wiskers [27,37] and nanowires [20,22,38]) embedded in metal matrices. (c) Evolution of the stress fraction carried by the W nanoribbons and the NiTi matrix as a function of applied strain upon the tensile loading. (d) Schematic of the elastic deformation distribution of the composite upon loading stage O-A.

Fig. 4a shows the evolution of the bearing stress of the W nanoribbons and the NiTi matrix during the tensile loading. The bearing stress of the nanoribbons was estimated by the function ($\bar{\sigma}_{11} = E^{\mathrm{hkl}}\,\varepsilon_{11}^{hkl}$) [39], whereas the Young's modulus of W along <110> used as reference state is E^{110} = 389 GPa [40], while the bearing stress of the NiTi matrix was calculated according to Mixture Law ($\sigma_{NiTi}=(\sigma_{appl}-\sigma_W\times V_W)/V_{NiTi}$). During the initial loading stage (O-A), the bearing stress of the W nanoribbons increased up to 5.1 GPa, more than 8 times as large as that of the NiTi matrix. Then the bearing stress of the W nanoribbons abruptly increased from 5.1 GPa to

10.8 GPa, while the bearing stress of the matrix decreased from 0.57 GPa to 0.42 GPa, when the matrix deformed by the SIMT. This result indicates that an immense load transfer from the matrix to the nanoribbons occur suddenly as the matrix underwent the SIMT, which exhibits obvious locality and rapidity. At the end of the loading (point C), the bearing strength of the W nanoribbons is estimated up to 11.6 GPa, which is over 8 times larger than that of the Nb nanowires in Cu matrix and even about twice as high as that of the Nb nanowires in the transforming NiTi matrix.

It is noted that the bearing strength of the W nanoribbons in the transforming NiTi matrix is also significantly higher than other known hard inclusions, no matter particulates [31,32], lamellae [24,33–36], whiskers [27,37] and nanowires [20,22,38] embedded in conventional metal matrices plastically deforming by dislocation slip, as shown in Fig. 3b. It is considered that the achievement of the ultrahigh bearing strength of the W nanoribbons may be attributed to the lattice strain matching at the atomic scale between the SIMT distortion (3~10%) of the matrix and the elastic strain of the nanoribbons [22]. The SIMT deformed via lattice shearing of the NiTi matrix can uniformly distribute stress on the W nanoribbons and expel stress concentration at nanoribbon-matrix interfaces, favoring to high effective load transfer from the matrix to the nanoribbons [24].

Fig. 4c shows the evolution of the load partitions of the W nanoribbons and the NiTi matrix during the tensile loading. In the initial loading stage (O-A), the stress fraction carried by the W nanoribbons decreased from ~25% to 20% with increasing the applied strain, indicating that a small amount of load was transferred from the W nanoribbons to the NiTi matrix. This result may be attributed to the uneven elastic deformations in the composite. It is evident that the W nanoribbons do not penetrate the entire composite along the wire axial direction, and the

Young's modulus of the W nanoribbons is much higher than that (~50 GPa [41]) of the NiTi matrix. For this situation, it is easy to understand that the elastic strain (ε'') of the matrix between the tips of two W nanoribbons was larger than that (ε') of the W nanoribbons during the initial elastic loading, as shown in Fig 4d. When the applied strain increased to 4.1%, it is seen that the stress fraction carried by the W nanoribbons abruptly increased from 20% to 45%, meanwhile the stress fraction carried by the NiTi matrix decreased from 80% to 55%. These indicate that a significant load transfer from the NiTi matrix to the W nanoribbons took place when the matrix underwent the SIMT. During the loading stage B-C, the stress fraction carried by W nanoribbons gradually decreased from 45% to 30%, while the stress fraction carried by NiTi matrix increased from 55% to 70%. For this, it is considered that the bearing stress of the NiTi matrix significantly increased during this deformation stage, while the bearing stress of the W nanoribbons remained almost constant (Fig. 4a), resulting in the decrease in the stress fraction carried by the nanoribbons. Overall, it is found that the stress fraction carried by the W nanoribbons with the volume fraction of 3% can be up to 45% for the strength of the composite.

4. Conclusion

An *in-situ* W-nanoribbons/NiTi-matrix composite was fabricated by mechanical reduction of a W-NiTi ingot. It is revealed that the large elastic deformation of the W nanoribbons in a NiTi matrix is dictated by and synchronized with the stress-induced martensitic transformation of the matrix. The bearing strength of the W nanoribbons, up to 11.6 GPa, was achieved in this composite. A significant load transfer from the matrix to the nanoribbons took place during the martensitic transformation of the matrix, exhibiting the characters of locality and rapidity. It is demonstrated that the stress fraction carried by the W nanoribbons with the volume fraction of 3% is up to 45% for the strength of the composite.

Corresponding Authors

*E-email: haoshijie99@163.com ,*E-email: lscui@cup.edu.cn.

Conflicts of interest

The authors declare no competing financial interest.

Acknowledgements

We thank Yadong Ru and Xing Fang for help in paper correction. This work was supported by the Key Program of the National Science Foundation of China (NSFC) (51731010), the NSFC (11474362, 51571212 and 51471187), and the Science Foundation of China University of Petroleum, Beijing (2462013YJRC005). The use of the Advanced Photon Source was supported by the US Department of Energy, Office of Science, and Office of Basic Energy Science under Contract No. DE-AC02-06CH11357.

References

[1] M. Estili, A. Kawasaki, Y. Pittini-Yamada, I. Utke, J. Michler, In situ characterization of tensile-bending load bearing ability of multi-walled carbon nanotubes in alumina-based nanocomposites, J. Mater. Chem. 21 (2011) 4272–4278. doi:10.1039/c0jm03906c.

[2] L. Huang, M. Qian, Z. Liu, V.T. Nguyen, L. Yang, L. Wang, J. Zou, In situ preparation of TiB nanowires for high-performance Ti metal matrix nanocomposites, J. Alloys Compd. 735 (2018) 2640–2645. doi:10.1016/j.jallcom.2017.11.238.

[3] Y.B. Tang, Y.Q. Liu, C.H. Sun, H.T. Cong, AlN nanowires for Al-based composites with high strength and low thermal expansion, J. Mater. Res. 22 (2007) 2711–2718. doi:10.1557/JMR.2007.0368.

[4] A. Wanner, D.C. Dunand, Synchrotron x-ray Study of Elastic Phase Strains in the Bulk of an Externally Loaded Cu/Mo Composite, Metall. Mater. Trans. A. 31 (2000) 2949–2962.

doi:10.1557/PROC-590-157.

[5] L. Xin, W. Yang, Q. Zhao, R. Dong, P. Wu, Z. Xiu, M. Hussain, G. Wu, Strengthening behavior in SiC nanowires reinforced pure Al composite, J. Alloys Compd. 695 (2017) 2406–2412. doi:10.1016/j.jallcom.2016.11.134.

[6] Y. Yue, P. Liu, Z. Zhang, X. Han, E. Ma, Approaching the theoretical elastic strain limit in copper nanowires, Nano Lett. 11 (2011) 3151–3155. doi:10.1021/nl201233u.

[7] G. Richter, K. Hillerich, D.S. Gianola, R. Mönig, O. Kraft, C.A. Volkert, Ultrahigh strength single crystalline nanowhiskers grown by physical vapor deposition, Nano Lett. 9 (2009) 3048–3052. doi:10.1021/nl9015107.

[8] T. Zhu, J. Li, S. Ogata, S. Yip, Mechanics of ultra-strength materials, MRS Bull. 34 (2009) 167–172. doi:10.1557/mrs2009.47.

[9] L. Huang, L. Wang, M. Qian, J. Zou, High tensile-strength and ductile titanium matrix composites strengthened by TiB nanowires, Scr. Mater. 141 (2017) 133–137. doi:10.1016/j.scriptamat.2017.08.007.

[10] Y. Jiao, L. Huang, L. Geng, Progress on discontinuously reinforced titanium matrix composites, J. Alloys Compd. 767 (2018) 1196–1215. doi:10.1016/j.jallcom.2018.07.100.

[11] B. Yang, N. Chen, G. Hao, J. Tian, K. Guo, Novel method to synthesize SiC nanowires and effect of SiC nanowires on flexural strength of Cf/SiC composite, Mater. Des. 52 (2013) 328–331. doi:10.1016/j.matdes.2013.05.087.

[12] Q. gang Fu, B. yi Tan, L. Zhuang, J. yi Jing, Significant improvement of mechanical properties of carbon/carbon composites by in situ growth of SiC nanowires, Mater. Sci. Eng. A. 672 (2016) 121–128. doi:10.1016/j.msea.2016.07.001.

[13] J. Lei, L. Zhou, Y. Tang, Y. Luo, T. Duan, W. Zhu, High-strength konjac

glucomannan/silver nanowires composite films with antibacterial properties, Materials (Basel). 10 (2017). doi:10.3390/ma10050524.

[14] Y. Dzenis, Structural Nanocomposites, 319 (2013). doi:10.1007/978-3-642-40322-4.

[15] R. Dong, W. Yang, P. Wu, M. Hussain, G. Wu, L. Jiang, High content SiC nanowires reinforced Al composite with high strength and plasticity, Mater. Sci. Eng. A. 630 (2015) 8–12. doi:10.1016/j.msea.2015.02.013.

[16] H.J. Ryu, S.I. Cha, S.H. Hong, Generalized shear-lag model for load transfer in SiC/Al metal-matrix composites, J. Mater. Res. 18 (2003) 2851–2858. doi:10.1557/JMR.2003.0398.

[17] Y. Lin, G. Ehlert, H.A. Sodano, Increased interface strength in carbon fiber composites through a ZnO nanowire interphase, Adv. Funct. Mater. 19 (2009) 2654–2660. doi:10.1002/adfm.200900011.

[18] X.Q. Liu, C.J. Li, J.H. Yi, K.G. Prashanth, N. Chawake, J.M. Tao, X. You, Y.C. Liu, J. Eckert, Enhancing the interface bonding in carbon nanotubes reinforced Al matrix composites by the in situ formation of TiAl3and TiC, J. Alloys Compd. 765 (2018) 98–105. doi:10.1016/j.jallcom.2018.06.170.

[19] P.M. Ajayan, J.M. Tour, Nanotube composites, 447 (2007) 1066–1068.

[20] L. Thilly, S. Van Petegem, P.O. Renault, F. Lecouturier, V. Vidal, B. Schmitt, H. Van Swygenhoven, A new criterion for elasto-plastic transition in nanomaterials: Application to size and composite effects on Cu-Nb nanocomposite wires, Acta Mater. 57 (2009) 3157–3169. doi:10.1016/j.actamat.2009.03.021.

[21] S. Ogata, Ideal Pure Shear Strength of Aluminum and Copper, Science (80-.). 298 (2002) 807–811. doi:10.1126/science.1076652.

[22] S. Hao, L. Cui, D. Jiang, X. Han, Y. Ren, J. Jiang, Y. Liu, Z. Liu, S. Mao, Y. Wang, Y. Li,

X. Ren, X. Ding, S. Wang, C. Yu, X. Shi, M. Du, F. Yang, Y. Zheng, Z. Zhang, X. Li, D.E. Brown, J. Li, A transforming metal nanocomposite with large elastic strain, low modulus, and high strength, Science (80-.). 339 (2013) 1191–1194. doi:10.1126/science.1228602.

[23] K. Otsuka, X. Ren, Physical metallurgy of Ti-Ni-based shape memory alloys, Prog. Mater. Sci. 50 (2005) 511–678. doi:10.1016/j.pmatsci.2004.10.001.

[24] J. Zhang, S. Hao, D. Jiang, Y. Huan, L. Cui, Y. Liu, H. Yang, Y. Ren, In situ synchrotron high-energy X-ray diffraction study of microscopic deformation behavior of a hard-soft dual phase composite containing phase transforming matrix, Acta Mater. 130 (2017) 297–309. doi:10.1016/j.actamat.2017.03.052.

[25] S.J. Hao, D.Q. Jiang, L.S. Cui, Y.D. Wang, X.B. Shi, Z.H. Nie, D.E. Brown, Y. Ren, Phase-stress partition and stress-induced martensitic transformation in NbTi/NiTi nanocomposite, Appl. Phys. Lett. 99 (2011). doi:10.1063/1.3629768.

[26] H.L. Sun, Z.X. Song, D.G. Guo, F. Ma, K.W. Xu, Microstructure and mechanical properties of nanocrystalline tungsten thin films, J. Mater. Sci. Technol. 26 (2010) 87–92. doi:10.1016/S1005-0302(10)60014-X.

[27] T.E. Wilkes, B.J. Harder, J.D. Almer, K.T. Faber, Load partitioning in honeycomb-like silicon carbide aluminum alloy composites, Acta Mater. 57 (2009) 6234–6242. doi:10.1016/j.actamat.2009.08.050.

[28] Z. Nie, Z. Wang, Y. Liang, D. Cong, G. Li, C. Zhu, C. Tan, X. Yu, Y. Ren, Y. Wang, Structural investigations of Fe-Ga alloys by high-energy x-ray diffraction, J. Alloys Compd. 763 (2018) 223–227. doi:10.1016/j.jallcom.2018.05.327.

[29] G.M. Michal, R. Sinclair, The structure of TiNi martensite, Acta Crystallogr. Sect. B Struct. Crystallogr. Cryst. Chem. 37 (1981) 1803–1807. doi:10.1107/S0567740881007292.

[30] M.L. Young, M.F.X. Wagner, J. Frenzel, W.W. Schmahl, G. Eggeler, Phase volume fractions and strain measurements in an ultrafine-grained NiTi shape-memory alloy during tensile loading, Acta Mater. 58 (2010) 2344–2354. doi:10.1016/j.actamat.2009.12.021.

[31] C. Tomchik, J. Almer, O. Anderoglu, L. Balogh, D.W. Brown, B. Clausen, S.A. Maloy, T.A. Sisneros, J.F. Stubbins, High energy X-ray diffraction study of the relationship between the macroscopic mechanical properties and microstructure of irradiated HT-9 steel, J. Nucl. Mater. 475 (2016) 46–56. doi:10.1016/j.jnucmat.2016.03.023.

[32] D.H. Bacon, L. Edwards, J.E. Moffatt, M.E. Fitzpatrick, Synchrotron X-ray diffraction measurements of internal stresses during loading of steel-based metal matrix composites reinforced with TiB2 particles, Acta Mater. 59 (2011) 3373–3383. doi:10.1016/j.actamat.2011.02.012.

[33] N. Jia, Z.H. Cong, X. Sun, S. Cheng, Z.H. Nie, Y. Ren, P.K. Liaw, Y.D. Wang, An in situ high-energy X-ray diffraction study of micromechanical behavior of multiple phases in advanced high-strength steels, Acta Mater. 57 (2009) 3965–3977. doi:10.1016/j.actamat.2009.05.002.

[34] B. Fu, W.Y. Yang, Y.D. Wang, L.F. Li, Z.Q. Sun, Y. Ren, Micromechanical behavior of TRIP-assisted multiphase steels studied with in situ high-energy X-ray diffraction, Acta Mater. 76 (2014) 342–354. doi:10.1016/j.actamat.2014.05.029.

[35] M.L. Young, J.D. Almer, M.R. Daymond, D.R. Haeffner, D.C. Dunand, Load partitioning between ferrite and cementite during elasto-plastic deformation of an ultrahigh-carbon steel, Acta Mater. 55 (2007) 1999–2011. doi:10.1016/j.actamat.2006.11.004.

[36] S. Roy, J. Gibmeier, A. Wanner, In situ study of Internal load transfer In a novel metal/ceramic composite exhibiting lamellar microstructure using Energy dispersive

synchrotron X-ray diffraction, Adv. Eng. Mater. 11 (2009) 471–477. doi:10.1002/adem.200800352.

[37] M.L. Young, J. DeFouw, J.D. Almer, D.C. Dunand, Load partitioning during compressive loading of a Mg/MgB2composite, Acta Mater. 55 (2007) 3467–3478. doi:10.1016/j.actamat.2007.01.046.

[38] S. Wang, L. Cui, S. Hao, D. Jiang, Y. Liu, Z. Liu, S. Mao, X. Han, Y. Ren, Locality and rapidity of the ultra-large elastic deformation of Nb nanowires in a NiTi phase-transforming matrix, Sci. Rep. 4 (2014) 17–20. doi:10.1038/srep06753.

[39] S. Harjo, N. Tsuchida, J. Abe, W. Gong, Martensite phase stress and the strengthening mechanism in TRIP steel by neutron diffraction, Sci. Rep. 7 (2017) 2–4. doi:10.1038/s41598-017-15252-5.

[40] J. Wang, Z. Zeng, C.R. Weinberger, Z. Zhang, T. Zhu, S.X. Mao, In situ atomic-scale observation of twinning-dominated deformation in nanoscale body-centred cubic tungsten, Nat. Mater. 14 (2015) 594–600. doi:10.1038/nmat4228.

[41] A. Ahadi, Q. Sun, Stress-induced nanoscale phase transition in superelastic NiTi by in situ X-ray diffraction, Acta Mater. 90 (2015) 272–281. doi:10.1016/j.actamat.2015.02.024.